

Fabrication of a Fractal Pattern Device for Focus Characterizations of X-ray Imaging Systems by Si Deep Reactive Ion Etching and Bottom-up Au Electroplating

ZHITIAN SHI,^{1,2,*} DANIEL JOSELL,³ KONSTANTINS JEFIMOV,¹ LUCIA ROMANO,^{1,2} THOMAS P. MOFFAT,³ MARCO STAMPANONI,^{1,2} CHRISTIAN M. SCHLEPÜTZ¹

¹Paul Scherrer Institut, 5232 Villigen PSI, Switzerland

²Institute for Biomedical Engineering, University and ETH Zürich, Zürich 8092, Switzerland

³Materials Science and Engineering Division, National Institute of Standards and Technology, Gaithersburg, Maryland 20899, USA

*Corresponding author: zhitian.shi@psi.ch

Received XX Month XXXX; revised XX Month, XXXX; accepted XX Month XXXX; posted XX Month XXXX (Doc. ID XXXXX); published XX Month XXXX

Abstract: Precisely aligned optical components are crucial prerequisites for X-ray tomography at high resolution. We propose a device with a fractal pattern for precise automatic focusing. The device is etched in a Si substrate by deep reactive ion etching and then filled by a self-terminating bottom-up Au electroplating process. The fractal nature of the device produces an X-ray transmission image with globally homogeneous macroscopic visibility and high local contrast for pixel sizes in the range of 0.165 μm to 11 μm , while the high absorption contrast provided between Au and Si enables its use for X-ray energies ranging from 12 keV to 40 keV.

Keywords: X-ray imaging; auto focusing; plasma etching; Au electroplating.

© 2021 Optica Publishing Group under the terms of the Optica Publishing Group Open Access Publishing Agreement

1. INTRODUCTION

High-resolution X-ray tomographic microscopy is one of the most powerful and sought-after 3D full field imaging methods for micro-scale structural investigations of virtually any material [1-6]. Thanks to the high flux of synchrotron radiation sources, high-quality measurements can be collected in a matter of minutes or even seconds, allowing for high throughput or time-resolved observations of the microstructure and its evolution in a sample [7-10]. Image quality and spatial resolution are critically dependent on achieving the best possible focus condition of the X-ray imaging system. Particularly in high-resolution X-ray imaging, the use of indirect X-ray detection systems is ubiquitous. X-rays are converted to visible light in a scintillator screen, and the resulting image on the scintillator is magnified onto an sCMOS image sensor via an optical light microscope, see Fig. 1(a)). Hence, the microscope optics must be carefully focused onto the scintillator, and the image plane of the scintillator needs to be precisely aligned perpendicular to the optical axis of the microscope. The focusing process can be done either manually by eye or with the aid of auto-focusing algorithms. In either case, being able to record a clear image with high-contrast features is prerequisite. Furthermore, to quantitatively evaluate and compare the local focus quality over the full field of view, a test image with macroscopically uniform and high visibility as well as

strong local contrast is required. For conventional imaging systems with visible light, a printed pattern can be placed in the imaging plane in front of the objective. For X-ray imaging systems, however, the image plane lies within the scintillator screen, and the focus test pattern must be generated by the X-ray beam itself using a test sample with good absorption contrast.

Normally, tomography beamlines possess a variety of optical microscopes and cameras, enabling X-ray imaging experiments at various different pixel sizes. For example, the TOMCAT beamline at the Swiss Light Source (SLS) uses five different types of optical microscopes with magnifications from 1 \times to 40 \times , and four different camera systems featuring native pixels sizes between 6.5 μm and 11.0 μm . Combining these cameras and microscopes provides effective pixel sizes ranging from 0.165 μm to 11.0 μm [8, 9]. To achieve a standardized focus quality evaluation, it is preferable to use a similar test image for all the different available configurations. The most commonly used patterns for focusing processes are chessboard patterns [11, 12], gratings [13], Siemens stars [14], and concentric circles [12]. The first two can produce a uniform contrast over a large area but only with a single characteristic length scale (the chessboard or grating period). The latter two can provide a range of feature sizes but are arranged around a specific point of interest and usually without self-similarity over larger length ranges. As a result, one typically requires a dedicated test pattern for

each combination of optical microscope and camera, with the commonly used patterns limited to cases where the pitch sizes are close to the effective pixel size.

Another option is to use random patterns, such like those generated, for example, by transmission through sandpaper [15]. These typically produce a range of image feature sizes related to the size of the randomly distributed structural features of the pattern. Statistically, they do provide long-range uniformity as long as the considered length scales are much larger than the feature sizes. However, they often lack a high enough contrast at high energies, or become too absorbing at low energies. Also, it is not easy to combine enough different feature sizes in a single test pattern to accommodate the full range of magnifications and energies. Often, the large structures required for the low magnifications cause severe illumination non-uniformities at higher magnifications. In practice, one therefore needs to use different characteristic feature sizes (grades of sandpaper) for different imaging conditions. Table 1 compares the capabilities of the different pattern designs mentioned above.

Table 1. Capabilities of the commonly used calibration patterns in X-ray imaging systems

Pattern	Acutance test	Resolution test	Zooming	Test area
Fractal	2D	discrete	Y	Full FoV
Siemens star	Omni	continuous	Y	Center only
Linear grating	1D	fixed	N	Full FoV
Chess-board	2D	fixed	N	Full FoV
Concentric circles	Omni	fixed	Y	Center only
Random (e.g.: sandpaper)	Omni	continuous	Y	Full FoV

This work presents an alternative based on the design and fabrication of a micro-structured pattern with a universal test pattern that fulfills the dual requirements of macroscopically homogeneous and high visibility as well as strong local contrast for the full range of pixel sizes and relevant X-ray energies.

2. PATTERN DESIGN

Figure 1 shows the schematics of the setup (a), and the design of the basic building blocks (b-c). The idea of the design is to produce a fractal pattern that features a hierarchy of feature sizes spanning the entire range of relevant length scales. The pattern is created in an iterative approach, with a basic building block represented by a black square (iteration 0). The next iteration of the pattern is then formed by surrounding the current iteration with eight inverted copies of itself. Iteration 1 thus consists of a central black square surrounded by eight white squares. This new 3×3 square array serves as the basic building block for the next iteration, which surrounds this central pattern with eight inverse copies to create a 9×9 array (see Fig 1(b)). This process can be repeated until the total size of the fractal pattern is larger than the required field of view.

Because the size of the pattern increases with each iteration, the above approach was modified to both reduce complexity of the

pattern to be written and improve flexibility in defining the overall patterned area. The size of the exposure file for the pattern to be written was thus limited to the original and inverse fractal patterns generated with 5 iterations (243×243 array = 486×486 μm), and the overall area of the substrate was covered using a 25×25 chessboard tiling of the two, as shown in Fig. 1(c), instead of simply iterating until the full area was covered.

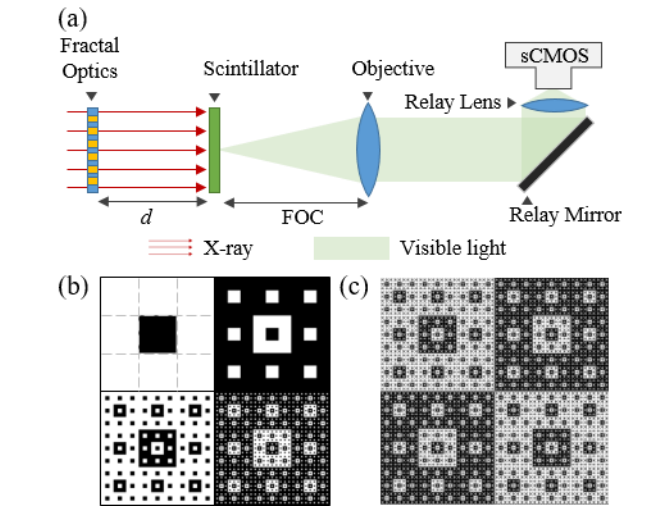


Fig. 1 (a) Schematic of the X-ray imaging system of the TOMCAT beamline at Swiss Light Source. (b) The fractal pattern at the 1st (top left), 2nd (top right), 3rd (bottom left), and 4th (bottom right) iterations. (c) Four fractal patterns made from 5th iterations, combined in a 2×2 chess-board arrangement.

To produce an X-ray imaging test pattern, the fractal pattern is transferred into a micro-fabricated device with high X-ray absorption contrast. Here, the basic square building block is represented by an etched square pit in a Si wafer that is filled with a highly absorbing metal, and its inverse corresponds to a Si square of the same size that has not been etched. The length chosen for the basic square building block was 2 μm, about 12 times larger than the smallest targeted image pixel size. The overall size of the required pattern equals the dimension of the detector, in pixels, multiplied by the largest effective pixel size, approximately 22 mm here.

Since the X-ray imaging takes advantage of the absorption contrast between different materials, the device is made of Si and Au – two materials with a substantial difference in their X-ray absorption properties. The target height for the Au filling was approximately 25 μm, which corresponds to one X-ray absorption length around 33 keV photons, thus providing a good absorption contrast throughout the full desired energy range.

3. EXPERIMENTS

A. Fabrication of the test sample

We fabricated the device using the 'litho-etch-electroplating' grating fabrication process [16], whose process flow is schematically shown in Fig. 2(a). We used a 4-inch N<100> double side polished Si wafer ($0.001\text{-}0.01\ \Omega\cdot\text{cm}$) as a substrate. The wafer was pretreated with pure O_2 plasma in a TePla 300 Plasma Processor and coated with a 50 nm layer of Cr etching hardmask in Evatec BAK evaporator. Finally, it was spin coated with a layer of AZ S1805 positive photoresist at a speed of 4000 rpm ($8000\pi\ \text{rad}/\text{min}$) and baked at $115\ ^\circ\text{C}$ for 90 s. A Heidelberg DWL66+ laser writer was used to expose the fractal pattern in the photoresist. Then the exposed photoresist was developed in MF-24A for 40 s. The resulting pattern in photoresist was transferred to the Cr layer by plasma etching, using Cl_2 and O_2 gases. The choice of etching method is not trivial for this pattern. In principle metal assisted chemical etching provides good anisotropy with no feature-dependent etching rate, but it is usually applied to etch interconnected features [17]. Since the fractal pattern in this study has many isolated features, we adapted the deep reactive ion etching (DRIE) method. The wafer was inserted into an Oxford PlasmaLab 100 ICP system, and etched with $\text{SF}_6/\text{C}_4\text{F}_8$ as etching/deposition gasses in deep reactive ion etching (Bosch process) [18]. However, due to the nature of the fractal pattern, the areas of the features to be etched vary substantially from each other. As a consequence, the DRIE process is affected by an obvious pattern scale microloading effect [18, 19], with shallower etch depth in smaller features, most particularly the isolated square pits shown as white dots in Fig. 1 (c). However, thanks to the microfabrication procedure the etched features are periodically reproduced with the same precision over the whole fabricated device area, which is the reason for a globally homogeneous visibility. A short O_2/SF_6 plasma treatment was used to remove the Teflon-like polymers from the surface of the etched Si template. The remaining Cr hard mask was removed with Cl_2/O_2 plasma and a final surface cleaning was performed using O_2 plasma. A top view SEM image of the resulted Si template is shown in Fig. 2(b). A bi-layer of 5 nm Al_2O_3 and 20 nm Pt was then conformally deposited by atomic layer deposition (BENEQ TFS 200) onto the Si template, with Al_2O_3 ensuring good adhesion and Pt providing a continuous electrically conductive layer for the subsequent Au electroplating step. The Au electrodeposition is divided into two sub-steps. The Si template was first conformally coated by Au electroplating with a layer of $\sim 50\ \text{nm}$ [16]. As conformal deposition cannot provide void-free filling of features having vertical sidewalls, let alone simultaneous filling of features having a variety of shapes and dimensions, this layer serves to facilitate Au nucleation for the subsequent bottom-up filling. The recessed features were filled with Au to the surface of the Si substrate using a bottom-up electrodeposition process [20-22]. The advantage of this method is that, despite the fully metallized surface, Au growth initiates at the very bottom of each recessed feature, and the bottom-up filling stops automatically, locally and universally, when the deposit reaches the surface of the Si substrate. This report is the first demonstration that this method can be utilized for simultaneous, void-free filling of structures whose features exhibit a wide range of shapes and sizes. Figure 2(c) shows a top view SEM image of a Au filled device. The largest continuous etched areas from the first to the fifth iteration are (4, 32, 256, 2048, and $16384\ \mu\text{m}^2$). The overall extent of the fabricated pattern covers an area of $24.3\times 24.3\ \text{mm}^2$. The Figure 2 (c) insert shows an SEM image of a cross-sectioned specimen with the Au filling. The etched Si depth varies in the range (19.7 to $27.8\ \mu\text{m}$) due to the microloading effect given the varying

feature area and shape. Despite this, the bottom-up Au electroplating process has achieved void-free fill in all the features up to the top surface of the substrate, with no chemical mechanical polishing used, nor needed, after the metal filling.

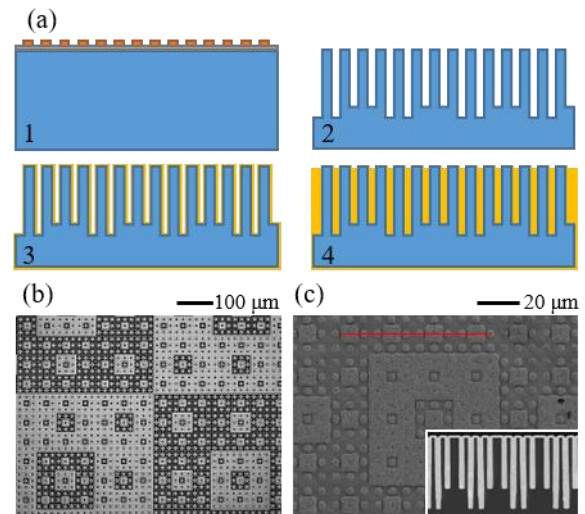


Fig. 2 (a) The process flow includes: (1) lithography; (2) plasma etching; (3) Pt pre-coating; and (4) bottom-up Au electroplating. Variation in feature depth is caused by the microloading effect. Top view SEM images of the device after (b) plasma etching and (c) Au electroplating. (c) (insert) Cross sectional SEM image taken from the test sample in the region marked with the red solid line (same scale bar), the Si template appears in dark gray and the brighter area is Au. The edge blurring induced by the slightly tapered sidewalls at the very bottom is not resolvable by the detectors, hence it does not affect the acutance. Bottom-up gold filling was achieved in an electrolyte comprised of $0.16\ \text{mol/L Na}_3\text{Au}(\text{SO}_3)_2 + 0.64\ \text{mol/L Na}_2\text{SO}_3$ with the addition of $50\ \mu\text{mol/L Bi}^{3+}$. Deposition was performed under potentiostatic condition at $-0.78\ \text{V}$ (versus $\text{Hg}/\text{Hg}_2\text{SO}_4/\text{saturated K}_2\text{SO}_4$ reference electrode) for 22 h 30 min as the workpiece was rotated at 200 rpm ($400\pi\ \text{rad}/\text{min}$).

B. Focus characterization with the fractal test sample

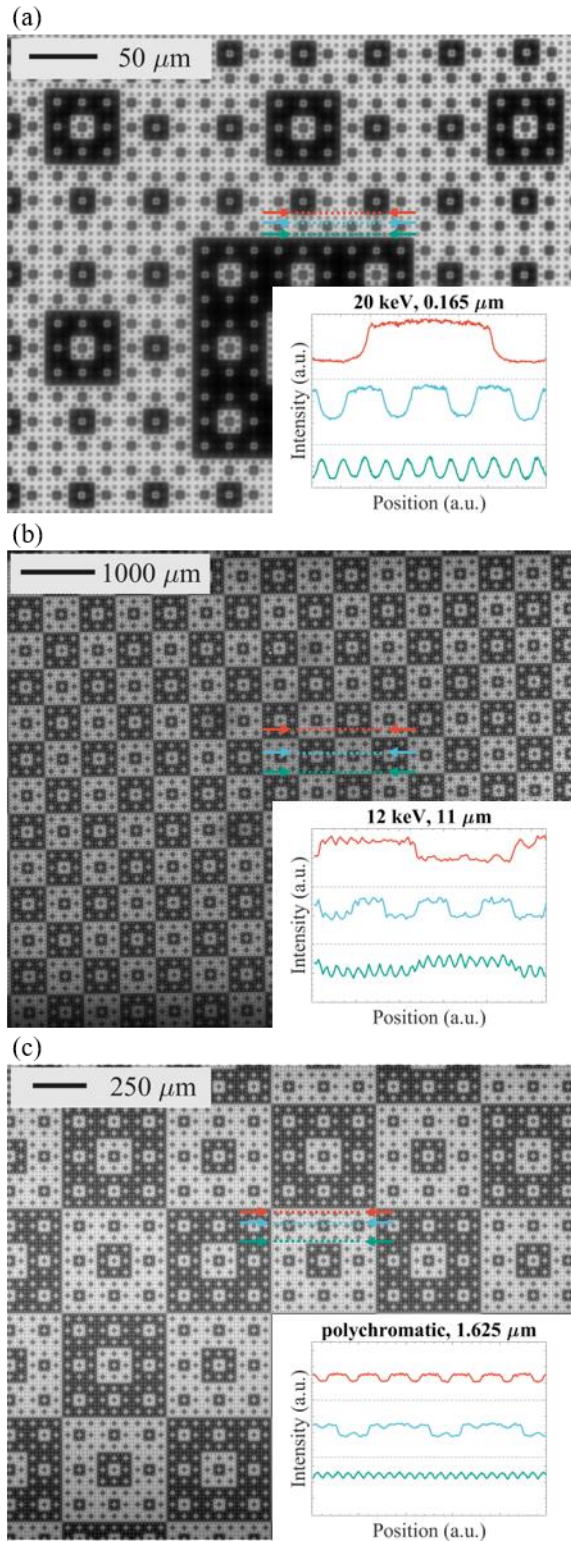


Fig. 3 X-ray transmission images of the test pattern taken at different X-ray energies and effective pixel sizes: (a) 20 keV, 0.165 μm ; (b) 12 keV, 11 μm ; (c) polychromatic X-ray beam, 1.625 μm . Variation of the Au thickness as a function of the pattern's feature size (see Fig 2(c)(insert)) causes a corresponding variation in the transmitted X-ray intensity with the size of the Au-filled feature. However, this variation should not compromise the

focus quantification, and the absorption contrast is sufficient to resolve the individual features across the full area.

The micro-fabricated focus test sample was tested in the TOMCAT beamline at the SLS with effective pixel sizes ranging from 0.165 μm to 11.0 μm for both monochromatic X-rays with energies between 12 keV and 40 keV as well as a polychromatic beam filtered with carbon (5 mm) and molybdenum (75 μm) with a lower cutoff around 15 keV and two spectral peaks at 20 keV and 37 keV. The distance d between the test sample and the scintillator is variable and can be adjusted to obtain the desired image quality. At near contact, the image is dominated by absorption contrast, while for larger distances, one starts to observe edge enhancement effects due to the refraction of the partially coherent beam. This increased acutance can be helpful to boost the local contrast, especially at higher energies where the absorption contrast begins to diminish. The test image produced by the sample can be observed with a clear and spatially homogeneous absorption contrast at all resolutions. Figure 3 shows transmission images acquired under representative imaging conditions. Note that the observable long-range variations in intensity (predominantly visible in the vertical direction) are due to an inhomogeneous X-ray beam profile and not caused by the pattern itself. The automatic focus is done by step scanning the objective lens, and the distance from the scintillator is denoted as FOC in Fig. 1(a).

Although the smallest micro-structural features cannot be resolved in the images with larger pixel sizes, the observed contrast pattern still resembles closely the fully resolved pattern at high resolution. The local image contrast is high under all conditions, albeit with the sub-micrometer sharpness of the transition between the Au and Si regions lost due to lateral light leakage within the luminescent material of the scintillator screen, and the long-range homogeneity is excellent. The micro-patterned device clearly achieves the desired properties of a universal focus characterization tool.

4. CONCLUSIONS

We present the fabrication and characterization of a micro-structured device featuring a fractal pattern designed for assessing the focus quality of indirect X-ray detection imaging systems. The device creates a uniform test pattern with high absorption contrast for hard X-rays (12 keV to 40 keV). The fractal design of the test sample ensures its universal use for setups that have different combinations of optical microscopes and cameras, providing different magnifications and resolutions. Its excellent long-range uniformity in combination with the high local contrast allows quantitative evaluation of the focus quality of the imaging system in a spatially resolved manner. This is made possible by the self-terminating, bottom-up Au electroplating, which allows uniform filling of the different shapes, sizes and depths of the recessed features in the patterns. This process could also be applied to several other applications that require Au microstructures with various thicknesses in the same device, such as vias, microelectromechanical systems (MEMS), etc.

Funding. This work has been partially funded by the ERC-2012-StG 310005 (PhaseX) grant, SNF_R'Equip grant 206021_189662 (SiDRY), the SNF-Sinergia Grants Nr. CRSII2_154472 and CRSII5_183568, the SNF Grant 159263, the Fondazione Gelu, the SwissLOS Fond of the Kanton Aargau, and SERI-AM-TTC.

Author contribution statement. Zhitian Shi: Si etching, original draft. Daniel Josell: Au electroplating, review & editing. Konstantins Jefimovs: review & editing. Lucia Romano: review & editing. Thomas P. Moffat: review & editing. Marco Stampanoni: Funding acquisition, review & editing, supervision. Christian M. Schlepütz: Conceptualization, characterization, review & editing, supervision.

Acknowledgments. The authors would like to thank the LMN-PSI for providing the facilities and professional support. We acknowledge Konrad Vogelsang and Helmut Schift (PSI) for laser writing and Didier Bouvet (CMi-EPFL) for the Al₂O₃/Pt ALD deposition. We acknowledge the Paul Scherrer Institut, Villigen, Switzerland for provision of synchrotron radiation beamtime at the TOMCAT beamline X02DA of the SLS. We acknowledge funding of the DWL 66+ from the ANAXAM in the framework of the Advanced Manufacturing—Technology Transfer Center (AM-TTC) alliance from the Swiss State Secretariat for Education, Research and Innovation (SERI). Corporate and product names are included for completeness of description only. Their inclusion is not intended to indicate that they are best suited for this process. Neither is it meant to imply NIST endorsement.

Disclosures. The authors declare no conflicts of interest.

Data availability. Data underlying the results presented in this paper are not publicly available at this time but may be obtained from the authors upon reasonable request.

References

1. N. E. Myrdis, "Advanced Tomographic Methods in Materials Research and Engineering, edited by J. Banhart," *Contemporary Physics* **51**, 374-374 (2010).
2. E. Borisova, G. Lovric, A. Miettinen, L. Fardin, S. Bayat, A. Larsson, M. Stampanoni, J. C. Schittny, and C. M. Schlepütz, "Micrometer-resolution X-ray tomographic full-volume reconstruction of an intact post-mortem juvenile rat lung," *Histochemistry and Cell Biology* **155**, 215-226 (2021).
3. J. A. Cunningham, I. A. Rahman, S. Lautenschlager, E. J. Rayfield, and P. C. J. Donoghue, "A virtual world of paleontology," *Trends Ecol. Evol.* **29**, 347-357 (2014).
4. F. Marone, C. M. Schlepütz, S. Marti, F. Fusses, A. Velásquez-Parra, M. Griffa, J. Jiménez-Martínez, K. J. Dobson, and M. Stampanoni, "Time Resolved in situ X-Ray Tomographic Microscopy Unraveling Dynamic Processes in Geologic Systems," *Frontiers in Earth Science* **7**(2020).
5. L. Wang, G.-Y. Yang, and L. X. Xu, "Synchrotron Radiation X-ray Imaging in Biomedical Research," in *Synchrotron Radiation in Materials Science* (2018), pp. 633-656.
6. H. Dejea, P. Garcia-Canadilla, A. C. Cook, E. Guasch, M. Zamora, F. Crispi, M. Stampanoni, B. Bijmens, and A. Bonnín, "Comprehensive Analysis of Animal Models of Cardiovascular Disease using Multiscale X-Ray Phase Contrast Tomography," *Sci. Rep.* **9**, 6996 (2019).
7. F. Marone, A. Studer, H. Billich, L. Sala, and M. Stampanoni, "Towards on-the-fly data post-processing for real-time tomographic imaging at TOMCAT," *Advanced Structural and Chemical Imaging* **3**, 1 (2017).
8. R. Mokso, C. M. Schlepütz, G. Theidel, H. Billich, E. Schmid, T. Celcer, G. Mikuljan, L. Sala, F. Marone, N. Schlumpf, and M. Stampanoni, "GigaFRoST: the gigabit fast readout system for tomography," *Journal of Synchrotron Radiation* **24**, 1250-1259 (2017).
9. J.-W. Buurlage, F. Marone, D. M. Pelt, W. J. Palenstijn, M. Stampanoni, K. J. Batenburg, and C. M. Schlepütz, "Real-time reconstruction and visualisation towards dynamic feedback control during time-resolved tomography experiments at TOMCAT," *Sci. Rep.* **9**, 18379 (2019).
10. F. Marone and M. Stampanoni, "Regridding reconstruction algorithm for real-time tomographic imaging," *Journal of Synchrotron Radiation* **19**, 1029-1037 (2012).
11. C. Dahmen, "Focus-based depth estimation in the SEM," in *Proc.SPIE*, (2008),
12. Y. Wang, X. Chen, J. Tao, K. Wang, and M. Ma, "Accurate feature detection for out-of-focus camera calibration," *Appl. Opt.* **55**, 7964-7971 (2016).
13. O. Yukitoshi, K. Fumio, M. Yasuhiro, and Y. Toru, "Three-dimensional profilometry based on focus method by projecting LC grating pattern," in *Proc.SPIE 7432*, *Optical Inspection and Metrology for Non-Optics Industries*, (2009), 743210.
14. W. T. Chen, A. Y. Zhu, V. Sanjeev, M. Khorasaninejad, Z. Shi, E. Lee, and F. Capasso, "A broadband achromatic metalens for focusing and imaging in the visible," *Nature Nanotechnology* **13**, 220-226 (2018).
15. K. M. Pavlov, D. M. Paganin, K. S. Morgan, H. Li, S. Berujon, L. Quénot, and E. Brun, "Directional dark-field implicit x-ray speckle tracking using an anisotropic-diffusion Fokker-Planck equation," *Phys. Rev. A* **104**, 053505 (2021).
16. K. Jefimovs, J. Vila-Comamala, C. Arboleda, Z. Wang, L. Romano, Z. Shi, M. Kagias, and M. Stampanoni, "Fabrication of X-ray Gratings for Interferometric Imaging by Conformal Seedless Gold Electroplating," *Micromachines* **12**, 517 (2021).
17. L. Romano and M. Stampanoni, "Microfabrication of X-ray Optics by Metal Assisted Chemical Etching: A Review," *Micromachines* **11**, 589 (2020).
18. Z. Shi, K. Jefimovs, L. Romano, and M. Stampanoni, "Towards the Fabrication of High-Aspect-Ratio Silicon Gratings by Deep Reactive Ion Etching," *Micromachines* **11**, 864 (2020).
19. S. Jensen and O. Hansen, "Characterization of the microloading effect in deep reactive ion etching of silicon," in *Micromachining and Microfabrication Process Technology IX*, (International Society for Optics and Photonics, 2003), 111-118.
20. D. Josell, Z. Shi, K. Jefimovs, L. Romano, J. Vila-Comamala, and T. P. Moffat, "Pushing the Limits of Bottom-Up Gold Filling for X-ray Grating Interferometry," *J. Electrochem. Soc.* **167**, 132504 (2020).
21. D. Josell, Z. Shi, K. Jefimovs, V. A. Guzenko, C. Beauchamp, L. Peer, M. Polikarpov, and T. P. Moffat, "Bottom-Up Gold Filling in New Geometries and Yet Higher Aspect Ratio Gratings for Hard X-ray Interferometry," *J. Electrochem. Soc.* **168**, 082508 (2021).
22. D. Josell and T. P. Moffat, "Bottom-up Filling of Damascene Trenches with Gold in a Sulfite Electrolyte," *J. Electrochem. Soc.* **166**, D3022-D3034 (2018).